Journal of Applied Fluid Mechanics, Vol. 17, No. 9, pp. 2061-2078, 2024.
Available online at www.jafmonline.net, ISSN 1735-3572, EISSN 1735-3645.
https://doi.org/10.47176/jafm.17.9.2456

Numerical Study of Erosion Wear Characteristics in a High-pressure Black Water Angle Valve by Using CFD-VOF-DPM Method

H. Jin[1,2], H. Xiang[1], M. Wang[1], R. Wen[1], X. Liu[1] and C. Wang[1†]

[1] *Department of Energy and Power Engineering, Faculty of Mechanical Engineering; Zhejiang Sci-Tech University, Hangzhou, Zhejiang, China*
[2] *Hefei General Machinery Research Institute Co., Ltd., Hefei, Anhui, China*

†Corresponding Author Email: wangchao@zstu.edu.cn

ABSTRACT

High-pressure black water angle valves are essential equipment of black water flash treatment systems in the coal gasification process, and they usually suffer from a high risk of erosion wear failure. In this study, computational fluid dynamics (CFD), combined with the discrete particle method (DPM) and the volume of fluid (VOF) method, was used to study the flow characteristics and erosion wear phenomenon in high-pressure black water angle valves under different valve cavity radii and opening angles. In particular, a new parameter, the drift index, was introduced to analyze the bias flow phenomenon in the throttling zone. With the increase in valve cavity radius, the drift index first decreases and then increases, and the influence of the valve cavity radius gradually weakens with the increase in the valve opening. It was found that, with the increase in valve cavity radius, the average erosion wear rate of the valve body decreases first and then increases. When the valve cavity radius was 132 mm, the average erosion wear rate of the valve body was the smallest. Therefore, the optimization of the valve cavity radius selection value can reduce the erosion wear damage of the high-pressure black water angle valve and increase its operational dependability.

Article History

Received November 22, 2023
Revised March 5, 2024
Accepted April 8, 2024
Available online July 2, 2024

Keywords:

DPM
Valve cavity radius
Multiphase flow
Drift index
Erosion wear

1. INTRODUCTION

Coal gasification is the core technology of deep coal processing and is an important technology for promoting the clean and efficient utilization of coal resources. In the process of coal gasification, a solid–liquid mixture (black water) with coal slag is discharged from the bottom of the gasifier and washing tower, which has high solid content, high temperature, and high hardness. The resource recovery and utilization of black water treatment systems can further improve the clean production level of coal gasification and achieve environmental protection and water conservation (Cao et al., 2020; Guo et al., 2022). A high-pressure black water angle valve is used to regulate the flash evaporation decompression process in the first stage of black water. Black water causes serious erosion wear on valve internals at high flow rates, leading to unplanned shutdowns and frequent accidents (Severiano et al., 2019). Therefore, it is important to analyze the failure process and optimize the structural design of high-pressure black water angle valves.

The erosion mechanism of multiphase flow on the wall surface is more complex and is often the synergistic effect of various factors. The relevant experimental conditions are difficult to control and lack predictability. Computational fluid dynamics (CFD) is widely used to study the erosion wear of solid particles with high accuracy and predictability (Mansouri et al., 2015; Espinoza-Jara et al., 2022; Wiedemann et al., 2023). Hou et al. (2011) conducted an experimental evaluation of the reaction of flow and cavitation under a specified opening of a high-pressure differential control valve using a data modeling system in CFD. The pressure distribution and critical cavitation flow rate in the flow field of a specified opening were obtained, and a scientific basis was provided for valve optimization and improvement. Qin et al. (2018) used CFD to simulate a pump-jet propulsor (PJP) with different tip clearances numerically and studied its influence on the hydrodynamic performance of the ejector. This provides an effective theoretical basis for improving the working efficiency and structural design optimization of PJPs. Yu et al. (2023) studied the flow characteristics and torque inside a ball valve using CFD software. The research showed that, the more streamlined the inner flow channel structure of the ball valve, the less likely it is to be

damaged by erosion wear, and the use of a large arc design is more conducive to prolonging the service life of the valve. Forder et al. (1998) used CFD to simulate a high-pressure black water angle valve numerically and found that the material flow rate was the main factor leading to valve wear failure. It was found that reducing the material flow rate under a constant pressure difference can optimize the structure of the high-pressure black water angle valve. Chen et al. (2022) studied the particle circulation characteristics of a conical fluidized bed by combining fluid mechanics and the discrete-element method (DEM). The flow dynamics of the particles are described from different perspectives. A method for defining particle circulation that considers the horizontal motion of particles was proposed, and the characteristics of particle circulation were revealed from the perspective of particle scale. Wallace et al. (2004) conducted a series of erosion wear simulations for cutoff and throttle valves using FLUENT. Parallel experiments verified that the flow information derived from the simulation experiment was basically consistent with the information obtained from the detection and that the area of loss completely matched the area of the specific experiment. Song et al. (2014) established a numerical model to study the hydrodynamic characteristics of a safety relief valve (SRV) combined with CFX code. In that study, detailed images of compressible fluid flow in a small area, including the valve seat, were obtained, providing high engineering value for the optimal design of SRVs. In summary, the application of CFD can compensate for the lack of predictability in experimental research and realize life prediction and structural optimization of the throttling device.

In recent years, researchers have continuously explored numerical simulation methods suitable for the characteristics of multiphase flows with phase changes. Related studies have shown that the CFD volume of fluid (VOF) discrete phase model (DPM) method is effective for simulating multiphase flow characteristics and erosion wear characteristics, including phase change (Zhang et al., 2018; Bambhania & Patel, 2022). Ban et al. (2021) used the VOF method to simulate the flow characteristics of an oil–gas slug flow in a horizontal straight pipe, calculated and captured the gas–liquid dynamic interface, and analyzed the pressure distribution, liquid holdup, and frequency of the slug flow. The numerical simulation method was validated by combining Baker's flow regime chart of a horizontal pipeline with relevant experimental data. Chen et al. (2022) used a numerical simulation method based on the VOF model and DPM to study the factors influencing erosion. Comparing the erosion of a 90° elbow under different conditions revealed that the erosion rate of the elbow under three-phase bubble flow was 7.5 times that under solid–liquid two-phase flow. Li et al. (1999) used the CFD-DPM-VOF method to simulate gas, liquid, and solid flows in a fluidized bed. The model can better capture the wake behavior, such as the bubble wake structure and shedding frequency. Kou et al. (2023) used CFD technology to simulate the mixing characteristics of a multiphase flow in an autoclave. The Euler–Euler model and DPM were used to study the solid holdup, critical suspension velocity, solid suspension inhomogeneity, gas holdup distribution, bubble trajectory, and residence time during the stirred leaching process in the autoclave. The accuracy of the numerical model was verified experimentally, and the experimental values agreed well with the simulation results. In summary, CFD technology can complete the study of multiphase flow characteristics, and the research results have high accuracy and predictability.

From the above, one can conclude that most research has focused on the factors influencing the fluid flow rate, solid particle concentration, and particle size. Few studies have considered the effect of fluid bias in the device on erosion wear. However, the fluid completes the rectification and confluence in the valve chamber of the high-pressure black water angle valve. Then, it flows into the throttling area between the valve core and the valve seat. The fluid flow state in the throttling area of a high-pressure black water angle valve typically changes significantly. The rectification effect of the fluid in the valve chamber directly affects the fluid flow rate at the orifice and the angle of the internals of the coal ash particle side impact valve. The rectification effect of the fluid in the valve chamber directly affects the fluid velocity distribution and changes the angle of the solid particle side impacting the valve internals. In this study, the CFD-VOF-DPM method was used to visualize the effect of the internal flow field of the valve, and the drift index was used to characterize the degree of fluid drift in the throttling area. The influence of the valve chamber radius and opening angle on the flow characteristics in the high-pressure black water angle valve was studied, which can provide a basis for reducing the failure degree of the valve and also provide a reference for ensuring stable operation of the high-pressure black water angle valve.

2. MODEL SETTING

2.1 Problem Description

In the process of coal gasification, a solid–liquid mixture with coal cinder (referred to as "black water") forms, and its solid content can reach as much as 4%. Black water must be treated by multistage decompression and vacuum flash evaporation to decompose its internal acidic components, achieve heat recovery and concentration, and realize resource utilization (Drew et al., 1979; Zheng et al., 2021). The process of the coal gasification black water treatment system is shown in Fig. 1. The high-temperature black water (approximately 519 K) discharged from the gasifier and scrubber is sent to the flash tank for heat exchange with the washing ash water, and the first stage of pressure reduction is performed when it passes through the high-pressure black water angle valve at the position marked in red in the figure.

2.2 Eulerian Model

The VOF model can simulate an immiscible multiphase flow by solving a separate equation and considering the volume fraction of each fluid passing through a region (Shirani et al., 2011; Li et al., 2023). Mass conservation is maintained in the solution process, which is more suitable for simulating the gas–liquid–solid

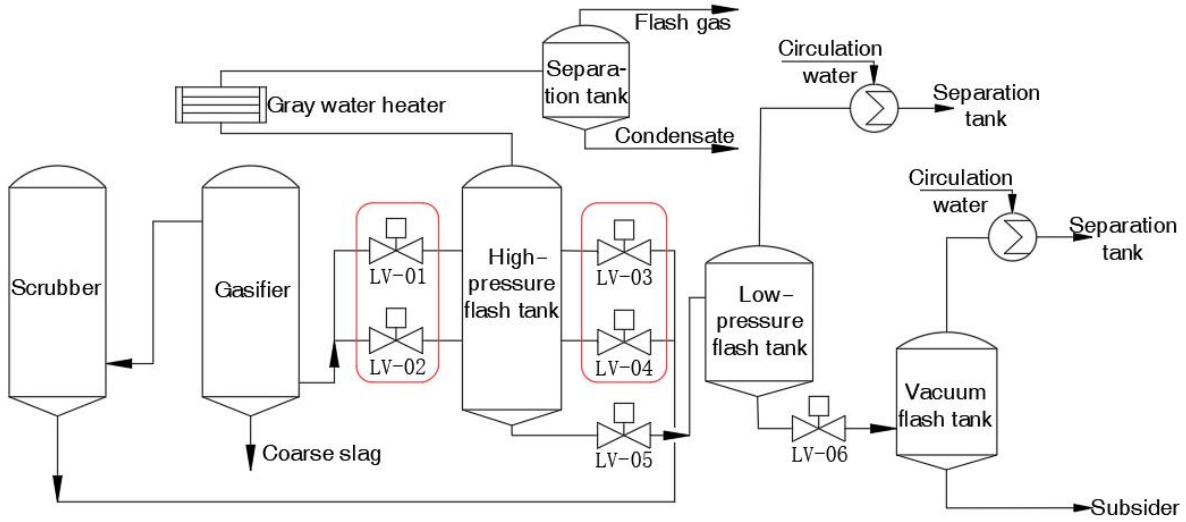

Fig. 1 Flow chart of coal gasification black water flash system

mixing process. The volume fraction continuity equation is (Tan et al., 2017)

$$\frac{\partial}{\partial t}(\alpha_q \rho_q) + \nabla(\alpha_q \rho_q \overrightarrow{u_q}) = 0 \tag{1}$$

where ρ_q, $\alpha_q$and$\overrightarrow{u_q}$ are the density, volume fraction and velocity of the phase q^{th}, respectively. The volume fraction of the primary phase was calculated using the following constraints:

$$\sum_{q=1}^{n} \alpha_q = 1 \tag{2}$$

The velocity field and energy equation of the solution of the momentum equation are shared by each phase and are expressed as

$$\frac{\partial}{\partial t}(\rho\vec{u}) + \nabla \cdot (\rho\vec{u}\vec{u}) = -\nabla \mathrm{p} + [\mu(\nabla\vec{u} + \nabla\vec{u}^{\mathrm{T}})] + \rho\vec{g} + \overrightarrow{F} \tag{3}$$

$$\frac{\partial}{\partial t}(\rho E) + \nabla \cdot \left(\vec{u}(\mathrm{p} + \rho E)\right) = \nabla \cdot \left(k_{eff} \nabla \mathrm{T}\right) + S_h \tag{4}$$

where ρ is the density of the mixed phase, p is the fluid pressure, $\vec{u}$ is the velocity of the mixed phase, μ is the viscosity of the mixed phase, $\vec{g}$ is the acceleration of gravity (9.8 $\mathrm{m/s^2}$), $\vec{F}$ is the additional momentum caused by the solid phase, k_{eff} is the effective thermal conductivity, S_h is the source term including radiation and other volume heat sources, and e is the total energy.

The physical parameters of the mixed phase are calculated as follows (Ganesan et al., 2017).

$$\rho = \rho_l \alpha_l + \rho_g (1 - \alpha_l) \tag{5}$$

$$\mu = \mu_l \alpha_l + \mu_g (1 - \alpha_l) \tag{6}$$

where α_l is the volume fraction of the liquid phase, ρ_l and μ_l are the liquid-phase density and kinematic viscosity, and ρ_g and μ_g are the gas-phase density and kinematic viscosity.

The evaporation–condensation model is a hydrodynamic model used to simulate and analyze the evaporation and condensation processes. The model can simulate complex fluid flows and heat transfer processes and provide quantitative prediction results for research (Kharangate & Mudawar, 2017). In this study, the depressurization flashing phenomenon of a fluid in a high-pressure black water angle valve was investigated, which is a nonequilibrium and heterogeneous fluid problem. Therefore, the Lee model for evaporation–condensation was used to calculate the depressurized flash in the high-pressure black water angle valve. The mass transfer equation between the gas and liquid phases is (Abbaspour et al., 2005)

$$\frac{\partial(\rho_g \alpha_g)}{\partial t} + \nabla \cdot \left(\rho_g \alpha_g \overrightarrow{u_g}\right) = \dot{m}_{lg} - \dot{m}_{gl} \tag{7}$$

where $\overrightarrow{u_g}$ is the gas-phase velocity, $\dot{m}_{lg}$ and $\dot{m}_{gl}$ are the mass transfer values caused by evaporation and condensation, respectively, and the mass transfer from the liquid phase to the gas phase is defined as positive.

When $T > T_{sat}$, the liquid phase evaporates:

$$\dot{m}_{lg} = coeff * \alpha_l \rho_l \frac{(T - T_{sat})}{T_{sat}} \tag{8}$$

When $T < T_{sat}$, the gas phase condensation is

$$\dot{m}_{gl} = coeff * \alpha_g \rho_g \frac{(T - T_{sat})}{T_{sat}} \tag{9}$$

Where T is the fluid temperature, T_{sat} is the saturation temperature, and $coeff$ is a time relaxation quantity.

$$coeff = \beta \sqrt{\frac{M}{2\pi R T_{sat}}} L \left(\frac{\rho_g \alpha_g}{\rho_l - \rho_g}\right) \tag{10}$$

where L is the latent heat (J/kg), R is the ideal gas constant, M is the vapor phase mass, β is defined by the adjustment coefficient and the physical properties of the steam, and 1.0 is taken under the condition of close equilibrium.

The saturation temperature T_{sat} and the saturation pressure always correspond to each other. To ensure the accuracy of the flash evaporation process simulation of high-temperature black water under a high pressure drop,

the tabular-pt-sat method (Chen et al., 2021) is used to call the table of self-set saturation temperature and saturation pressure data points to specify the saturation temperature. The saturation temperature uses the dichotomy and local linear interpolation to determine the target value based on the saturation pressure.

The realizable k–ε model is suitable for addressing flow separation and complex secondary flow problems (Wen et al., 2022). Owing to the problem of fluid flashing and backflow in the high-pressure black water angle valve in the simulation, the realizable k–ε turbulence model is selected. The turbulent kinetic energy and dissipation rate transport equations are as follows (Chowdhury et al. 2022):

$$\rho\frac{dk}{dt}=\frac{\partial}{\partial x_i}\left[\left(\mu+\frac{\mu_t}{\sigma_k}\right)\frac{\partial k}{\partial x_i}\right]+G_k+G_b-\rho\varepsilon-Y_M \tag{11}$$

$$\rho\frac{d\varepsilon}{dt}=\frac{\partial}{\partial x_i}\left[\left(\mu+\frac{\mu_t}{\sigma_\varepsilon}\right)\frac{\partial \varepsilon}{\partial \sigma_\varepsilon}\right]+\rho C_1 S\varepsilon-\rho C_2\frac{\varepsilon^2}{k+\sqrt{v\varepsilon}}+C_{1\varepsilon}\frac{\varepsilon}{k}C_{3\varepsilon}G_b \tag{12}$$

In the above formula, $C_1=max[0.43,\frac{\eta}{\eta+5}]$, and $\eta=S\frac{k}{\varepsilon}$. Here, k is the turbulent kinetic energy, ε is the dissipation rate, μ is the viscosity of the continuous phase, v is the kinematic viscosity of the continuous phase, μ_t is the turbulent viscosity coefficient, S is the average strain rate, G_k is the turbulent kinetic energy generated because of the average velocity gradient, and G_b is the turbulent kinetic energy generated owing to the influence of buoyancy. In addition, Y_M represents the effect of pulsating expansion of compressible flow on the total dissipation rate, $C_{1\varepsilon}$, C_2, and $C_{3\varepsilon}$ are constants, and σ_k and σ_ε are the turbulent Prandtl numbers of kinetic energy and its dissipation rate, respectively. The general values are: $C_{1\varepsilon}$=1.44, C_2=1.9, $C_{3\varepsilon}$=0.09, σ_k=1.0, and σ_ε=1.2.

2.3 Discrete-Phase Model

The Lagrange method is used to calculate particle trajectories. The solid particles are regarded as discrete phases, and the interaction between the discrete and continuous phases is considered in the calculations. In this study, the volume fraction of particles was less than 10%, so it was not necessary to consider the interactions between bubbles and particles. In the DPM model, to solve the discrete-phase particle motion trajectory, it is necessary to integrate the differential equation describing the particle force. According to Newton's law, the inertia of a particle is equal to the sum of the forces acting on it. In the Cartesian coordinate system, the force balance equation of the particle is

$$\frac{du_p}{dt}=\frac{\vec{u}-\vec{u}_p}{\tau_r}+\frac{\vec{g}(\rho_p-\rho)}{\rho_p}+\overrightarrow{F_w} \tag{13}$$

where $\overrightarrow{F_w}$ is an additional acceleration term (including virtual mass and pressure gradient forces) of the particles. Here, $F_D=\frac{\vec{u}-\vec{u}_p}{\tau_r}$ is the drag force on the particles (Peng et al., 2013; Wang & Shen, 2023):

$$\tau_r=\frac{\rho_p d_p^2}{18\mu}\frac{24}{C_d Re} \tag{14}$$

$$\mathrm{Re}=\frac{\rho d_p|\vec{u}-\vec{u}_p|}{\mu} \tag{15}$$

where u is the velocity of fluid flow, $\vec{u}$ is the particle velocity, ρ_p is the particle density, ρ is the continuous phase density, d_p is the particle diameter, Re is the particle Reynolds number, and C_d is the spherical drag coefficient, which is defined as (Alghurabi et al., 2021)

$$C_d=a_1+\frac{a_2}{Re}+\frac{a_3}{Re} \tag{16}$$

The value of a_i is the coefficient derived by Zhang et al. (2010).

The flow field of the high-pressure black water angle valve studied has a large pressure gradient, large velocity gradient, and high particle concentration. Therefore, the virtual mass force in Eq. (17) and pressure gradient force in Eq. (18) of the discrete-phase particles must be considered in the calculation (Zamani et al., 2017).

$$\overrightarrow{F_{vm}}=\rho\frac{\Pi d_p^3}{12}(\vec{u}-\vec{u}_p) \tag{17}$$

$$\overrightarrow{F_p}=\frac{\rho}{\rho_p}\overrightarrow{\nabla u}\vec{u}_p \tag{18}$$

where $\vec{u}$ is the continuous-phase velocity, $\vec{u}_p$ is the particle velocity, ρ_p is the particle density, ρ is the continuous-phase density, and d_p is the particle diameter.

2.4 Particle Erosion Model

In CFD calculations, the particle wall rebound model is usually combined with the erosion model to solve the particle motion, erosion rate, and erosion position. In addition, the normal restitution coefficient e_n and tangential restitution coefficient e_n are set on the wall to describe the changes in the particle impact velocity. In this study, the impact rebound recovery coefficient function of the variable of impact angle θ was that proposed by Forder et al. (1998), and its expression is

$$e_n=0.998-0.78\theta+0.19\theta^2-0.024\theta^3+0.027\theta^4 \tag{19}$$

$$e_t=1-0.78\theta+0.84\theta^2-0.21\theta^3+0.028\theta^4-0.022\theta^5 \tag{20}$$

The CFD-DPM model can obtain the erosion wear rate and wear distribution of the particles on the wall by selecting the impact data, such as the impact velocity v and the impact angle θ, of the particles with a certain impact velocity. The application scope of each erosion model was compared by analyzing the different erosion models proposed previously (Parsi et al., 2014). In this study, the particle erosion and accretion model was used to simulate the erosion, and the erosion wear rate ($kg\cdot m^{-2}\cdot s^{-1}$) is defined as (Zheng et al., 2016; Alghurabi et al., 2020)

$$R_{\text{erosion}}=\sum_{p=1}^{N_P}\frac{\dot{m}_p C(d_p)f(\theta)v^{b(v)}}{A_f} \tag{21}$$

where $\dot{m}_p$ is the particle mass flow rate (kg/s), $f(\theta)$ is the impact angle function (rad), v is the particle impact velocity (m/s), $b(v)$ is the relative velocity function, $C(d_p)$ is the particle diameter function, which is generally a constant of 1.1E-10, A_f is the erosion area on the wall (m^2), and N_p is the number of particles that collide with the surface of the eroded material.

In the particle erosion wear model, $b(v)$and $f(\theta)$ are necessary conditions for accurate estimation of erosion wear, and they are related to particle impact data and particle and target characteristics. The surfaces of the valve core and seat of the high-pressure black water angle valve were made of tungsten carbide (WC). Zheng et al. (2016) built a gas–solid erosion test bench to simulate the erosion characteristics of samples coated with WC with Co binder in the temperature range of 20°C–400°C, the particle impact angle range of 10°–90°, and the particle (pulverized coal) impact velocity range of 0–200 m/s. The erosion rate of the sample was normalized to obtain $f(\theta)$ and $b(v)$, which were used to calculate the relative erosion rate of the WC coating at different impact angles. When the impact angles θ are 0°, 15°, 30°, 45°, 60°, 75°, and 90°, the values of $f(\theta)$ are 0, 0.1, 0.31, 0.61, 0.9, 1, and 0.82, respectively. The value of $b(v)$ is 2.3.

3. FLUID DOMAIN AND CALCULATION METHOD

3.1 Fluid Domain Geometric Model

The geometric structure of a high-pressure black water angle valve is shown in Fig. 2. The valve is composed of a valve core, valve stem, valve seat, valve cavity, and so on. In the valve chamber, the valve core and seat form a throttling part. The radius of the valve cavity (R) was the research variable in this study, and its specific position is shown in Fig. 2. The differences in fluid flow characteristics in the valve when the valve cavity radii were 129, 132, 135, 138, and 141 mm were compared and analyzed. The CFD model of the valve is shown in Fig. 3, where the fluid flows through the valve seat to the buffer tank. To make the simulation state as close as possible to the actual state and the flow field more stable, the inlet and outlet flow channels were extended appropriately. The valve seat was connected to a pneumatic actuator to control the valve opening. The opening was defined by the valve stroke. According to the practical application of the high-pressure black water angle valve (Zheng et al., 2016; Yan et al., 2021), the openings were selected as 20%, 40%, 60%, and 80% for this research.

3.2 Boundary Condition

In this study, the boundary conditions of the numerical simulation were set according to practical application data (Zheng et al., 2016). The pressure implicit with splitting of operators algorithm was used to solve the coupling of pressure and velocity. Combined with the actual operation of a factory, the inlet and outlet pressures were set to pressure inlet and outlet values of 6.33 and 0.8 MPa, respectively. The temperatures of the fluid inlet and outlet interface were 519 and 448 K, respectively. The near-wall flow was solved by the standard wall function

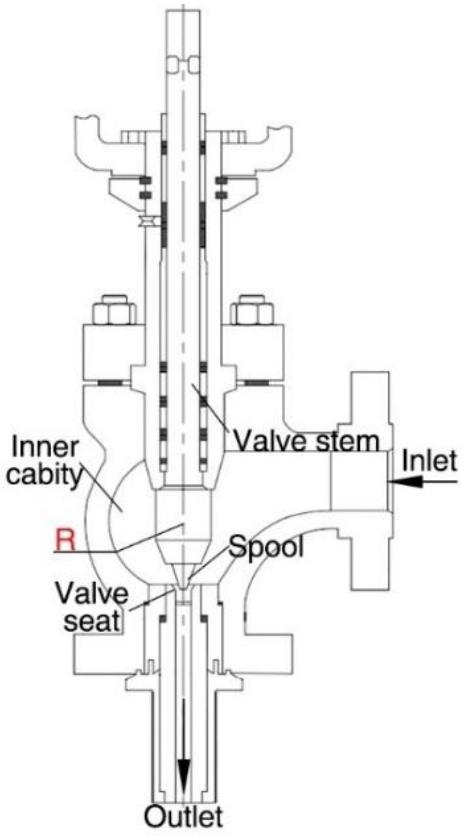

Fig. 2 Internal structure diagram of the high-pressure black water angle valve

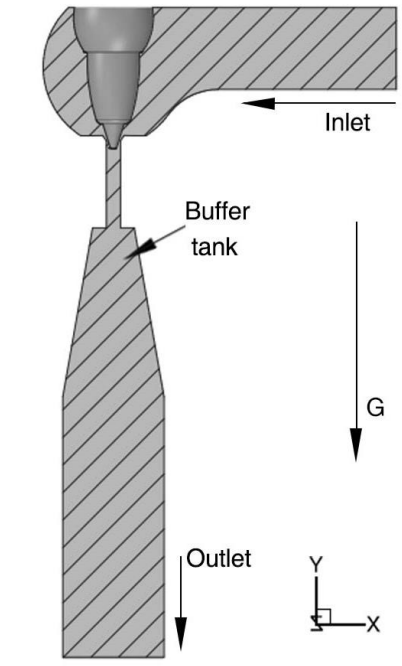

Fig. 3 Geometric model

method, and the inner wall surface adopted the nonslip boundary condition. Combined with the actual flow medium of the high-pressure black water angle valve, water was selected as the flow medium in the simulation, and flash evaporation occurred under a high-pressure

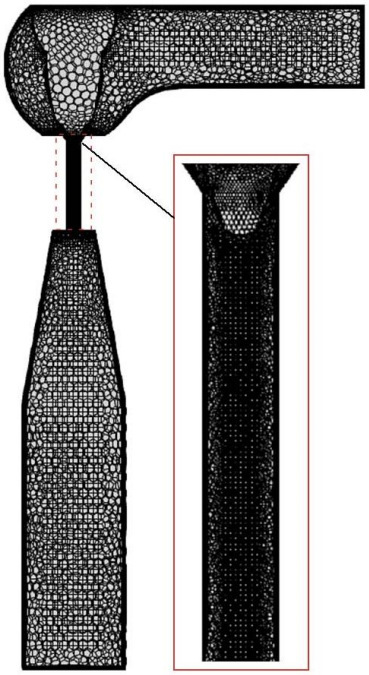

Fig. 4 High-pressure black water angle valve and throttling area grid division result diagram

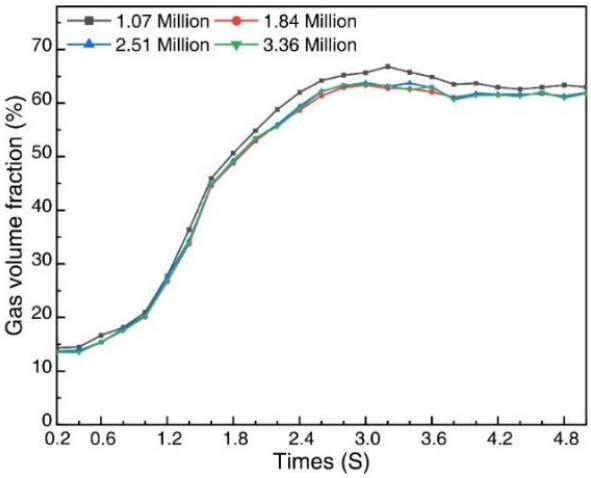

Fig. 5 Comparison of the average volume fraction values of the gas phase in the flashing region

Fig. 6 Valve core erosion wear failure diagram

difference. Anthracite particles were selected as solid particles. The particle shape was spherical, the particle size was 0.75 μm, and the mass flow rate at the inlet was set to 0.55 kg/s.

3.3 Mesh Independence and Model Verification

An unstructured hybrid grid was used to divide the model grid. A thicker grid was adopted for straight sections of the inlet and outlet. The flow field characteristics of the valve throttling area change drastically and must be encrypted locally. The division of the computational domain grid is shown in Fig. 4. Grid independence verification is important for ensuring the credibility of the calculation results. Four grids of approximately 1.07 million, 1.84 million, 2.51 million, and 3.36 million were created by selecting a 132 mm valve chamber radius under an extreme opening of 20%. The calculation was performed according to the boundary conditions described in Section 3.2. To evaluate grid independence, the average volume fraction of the gas phase in the flashing region was obtained using the integral, which changes with the calculation time. The calculation results are shown in Fig. 5.

The calculation results show that, when the grid number is 1.07 million, the calculation accuracy of the average volume fraction of the gas phase is low. The calculation results are significantly different from those for other grid numbers. This is because of the small difference in the calculation results for the number of remaining grids. This ensures the accuracy of the calculation results and improves the calculation efficiency. Finally, 1.84 million grids were selected for the numerical research.

High-temperature black water has a high solid content. During system operation, the solid particles strongly impact the wall of the high-pressure black water angle valve. Under the long-term erosion and wear of solid particles, a large area of damage will occur at the connection between the valve core head and the throttling area. In practical engineering applications, the erosion wear failure of a valve core head is distributed over a long strip, as shown in Fig. 6. The wear rate distribution of the valve core obtained by the numerical simulation under the calculation conditions set in this study is shown in Fig. 7. The parts with higher erosion wear rates are mainly concentrated in the head of the valve core and distributed in flakes. The actual failure of the high-pressure black water angle valve was compared with the results predicted by the numerical model. The numerical simulation results were consistent with the actual failure situation.

To verify further the accuracy of the numerical simulation model used, it was compared with the experimental data obtained by Shao et al. (2023), who experimentally measured the erosion wear rate of a nozzle at an observation point. The fluid at the inlet of the nozzle was pressurized by the pump to 10 MPa, the particle

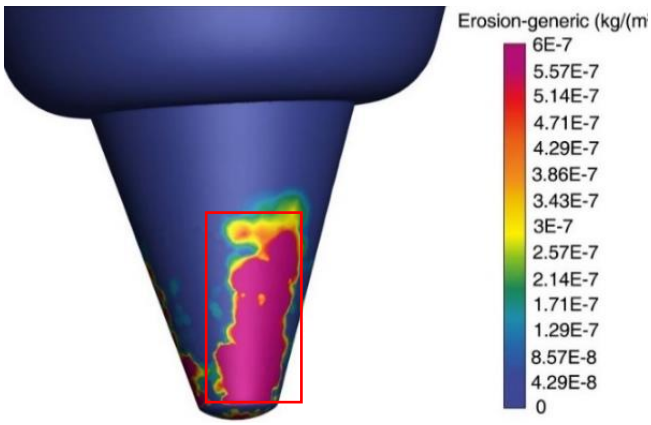

Fig. 7 Valve core erosion wear rate distribution nephogram

(a) CFD meshing and location of the measurement points

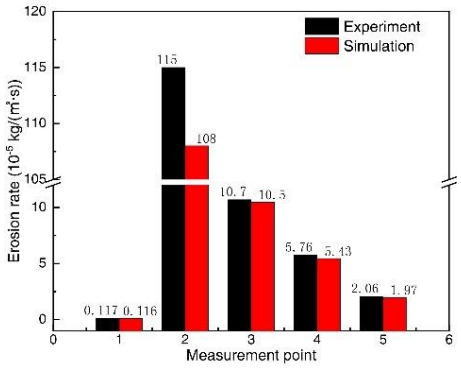

(b) Comparison between the experimental data and the simulation results

Fig. 8

concentration in the abrasive was 10%, and the experiment was continued for 1800 s. The same three-dimensional nozzle model was constructed as the experimental device, and the same parameters were set for the numerical simulation to verify the accuracy of the numerical simulation model used in this study. Figure 8 (a) includes the three-dimensional geometry of the nozzle and the distribution of the measurement points. Figure 8(b) shows a comparison of the erosion wear rates between the five measurement points. The deviations between the experimental data and the numerical simulation results were 0.8 %, 6.08 %, 2.71 %, 5.43 %, and 4.36 %, respectively. The maximum error value is 6.08 %, which is less than 7 %. Therefore, the numerical simulation model is highly reliable and applicable.

4. RESULTS AND DISCUSSION

In this study, a numerical simulation structure of a high-pressure black water angle valve was analyzed. The flow characteristics of the fluid in the valve were analyzed with respect to the gas volume fraction, fluid drift index, velocity distribution, and erosion wear rate distribution. The influence of the valve chamber radius on the flow characteristics of the high-pressure black water angle valve was examined.

4.1 Flashing Characteristics

When high-temperature black water flows through the throttling part, the fluid pressure downstream of the throttling part decreases sharply and flashes. The gas-phase distribution in the flashing region tends to be stable during the full development stage of the continuous phase (Yadigaroglu & Zeller, 1994). Based on the content in Section 3.3, the gas-phase distribution cloud diagram when the flow field calculation time is t = 6 s was selected to analyze the flashing characteristics in the valve. The flow field in the flash evaporation area of the high-temperature black water was more disordered, and the flow velocity increased sharply. The erosion wear effect of solid particles on the wall surface intensified. Figure 9 shows the gas-phase fraction diagram of different openings when the valve cavity radius was 132 mm. The fluid had different degrees of phase change at the head of the spool, the throttling area, and the downstream position of the valve seat outlet. The medium in the valve began to flash in a large area after flowing out of the throttling area, and the gas phase was distributed around the main flow area. The gas phase in the throttling area was mostly distributed near the wall. With an increase in the opening degree, the position of flash evaporation began to move down gradually.

Instantaneous superheating and instantaneous pressure drop are the two driving forces of flash evaporation. When the fluid flows through the high-temperature black water angle valve, the pressure and temperature decrease by 5.43 MPa and 71 K, respectively. Therefore, the instantaneous pressure drop is the driving force for fluid flashing in the high-pressure black water angle valve. Figure 10 shows the pressure distribution of the medium in the valve at different openings at t = 6 s when the radius of the valve chamber is 132 mm. The analysis shows that the medium in the valve has an instantaneous pressure drop in the throttling area, and the pressure gradually increases from the upstream position of the valve seat to the outlet pressure value. The pressure of the spool head changes drastically, and, as the opening increases, the pressure change gradually slows. Figure 9 reveals that, under the same working conditions, the more severe the fluid pressure change, the higher the degree of fluid flashing in the valve.

In summary, the flashing intensity of the flow field is proportional to the average gas volume fraction and pressure difference in the fluid domain. To compare and analyze the influence of the valve cavity radius on the medium flash intensity, the curve of the average gas volume fraction in the flashing zone with respect to the radius of the valve chamber at different openings is shown in Fig. 11. The variation trend of this variable is essentially the same for different openings. With an increase in the radius of the valve cavity, the gas-phase volume fraction increases overall. The minimum value occurs at a radius

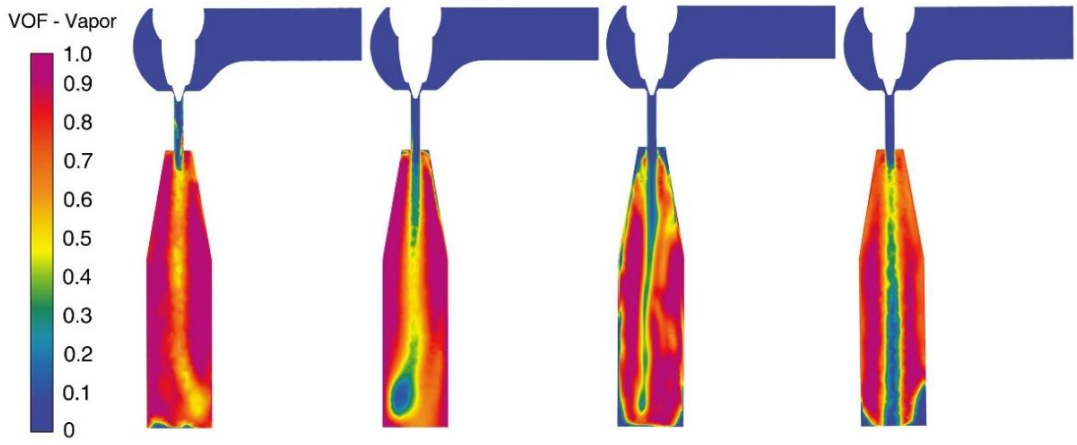

(a) 20% (b) 40% (c) 60% (d) 80%

Fig. 9 Gas-phase fraction diagram of the medium in the valve at different openings when the valve chamber radius is 132 mm

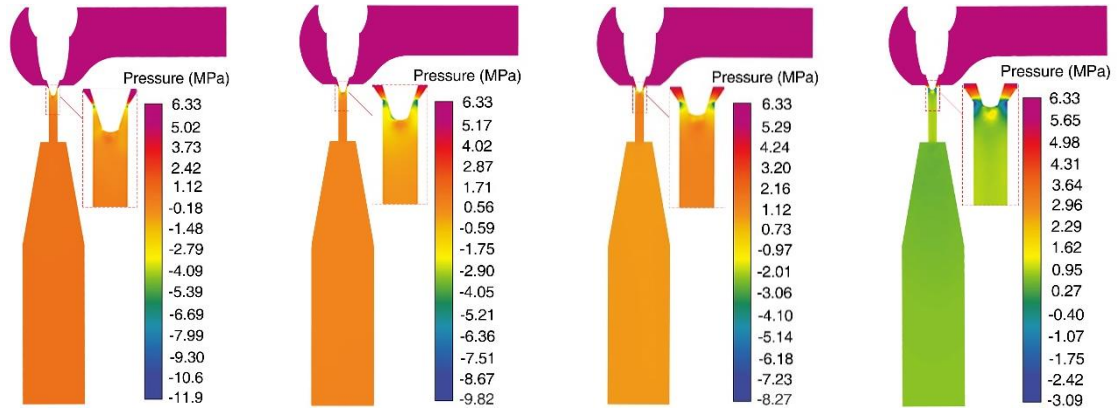

(a) 20% (b) 40% (c) 60% (d) 80%

Fig. 10 Static pressure distribution of the medium in the valve under different openings when the valve cavity radius is 132 mm

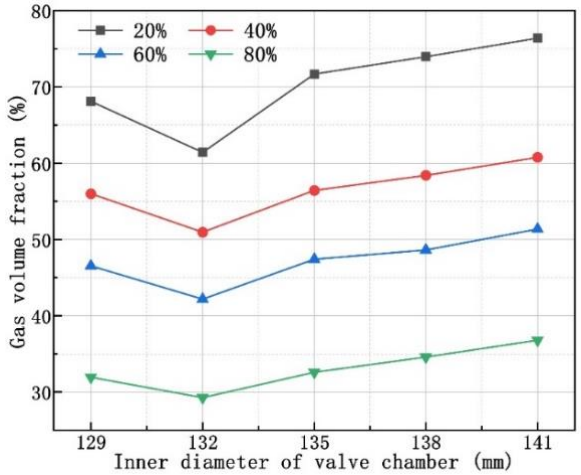

Fig. 11 Variation of the average gas volume fraction with the radius of the valve chamber in the flash zone with different openings

of 132 mm, and the flashing intensity is the lowest. Under different opening degrees, the maximum difference in the average gas-phase volume fraction under different valve cavity radii varies. Meanwhile, as the opening increases, the influence of the valve chamber radius on the flash intensity of the flow field gradually weaken. For openings of 20%, 40%, 60%, and 80%, the maximum differences in average gas volume fraction under different valve cavity radii are 14.98%, 10.27%, 9.18%, and 7.62%, respectively. However, the minimum value for an 80% opening is 29.3 %, which is only 2.78 times the average value of the maximum difference caused by the valve cavity radius. Therefore, an appropriate valve cavity radius can reduce the flashing intensity of the fluid in a high-pressure black water angle valve. This slows the erosion and wear of the flow medium on the valve internals.

4.2 Flow Characteristics

Figure 12 shows the internal velocity cloud diagram of the flow field and velocity vector amplification diagram of the throttling area at different openings when the valve cavity diameter is 132 mm. The velocity of the fluid in the throttling area changes drastically, and the change amplitude is approximately 170 m/s. As the flow area changes, the flow rate gradually decreases along the flow direction. The flow field in the front area of the throttling and downstream parts of the buffer tank is relatively stable, and the maximum change in the velocity is only 35 m/s, which is much smaller than that in the throttling area. In addition, under the action of the pressure difference, the

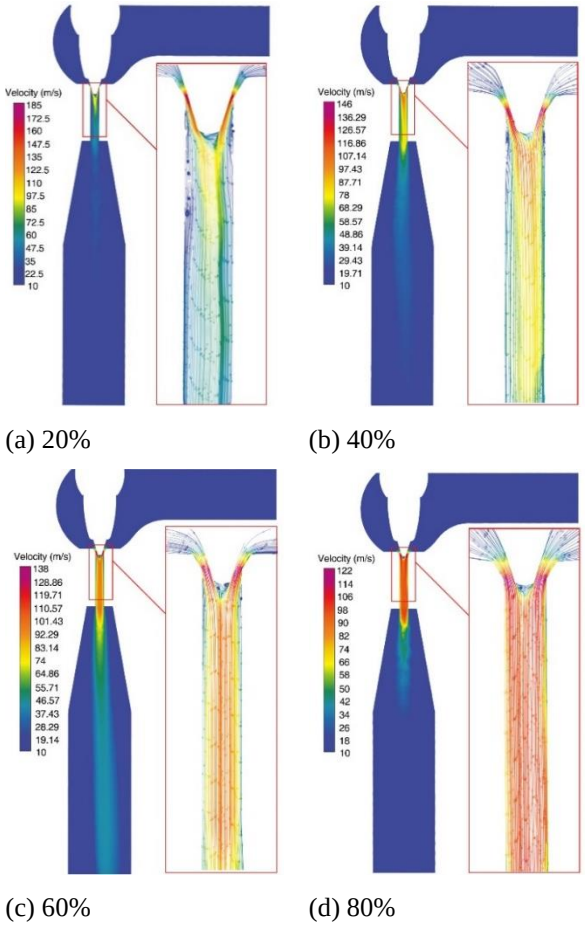

(a) 20% (b) 40%

(c) 60% (d) 80%

Fig. 12 Velocity distribution c of the medium in the valve in the valve at different openings when the radius of the valve cavity is 132 mm

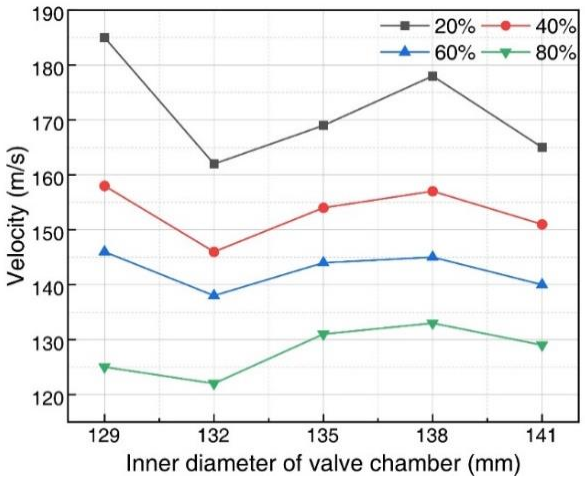

Fig. 13 Variation curve of the maximum speed of the high-pressure black water angle valve at different openings with the radius of the valve chamber

medium in the valve exhibits a bias flow and eddy current phenomenon in the throttling area, and the particles in the fluid strongly impact the valve body wall, resulting in serious erosion and wear damage.

According to erosion wear theory, a fluid with the same solid content affects the target at the same impact angle. The greater the impact velocity, the stronger the impact of solid particles (Humphrey, 1990). The maximum flow velocities under different opening degrees and valve cavity radii were compared and analyzed, and the change trend is shown in Fig. 13. The value of the valve cavity radius has different degrees of influence on the maximum value of the fluid because of the influence of the opening. However, for different opening degrees, the maximum value of the fluid exhibits the same trend as the radius of the valve cavity. With a gradual increase in the opening degree, the fluctuation of the maximum flow velocity with the change in the valve cavity radius gradually slows. Under openings of 20%, 40%, 60%, and 80%, the differences in the maximum flow velocity are 16, 12, 11, and 10 m/s, respectively, when the valve cavity radii are 129, 132, 135, 138, and 141 mm. As the opening increases, the influence of the valve chamber radius on the flow field gradually weakens. However, under an 80% maximum opening, the difference in the maximum flow velocity under different valve chamber radii remains 10 m/s.; therefore, the value of the valve cavity radius has a significant influence on the impact of particles.

Flow velocity is not the only factor that determines the fluid erosion wear effect. At the same flow rate, the higher the stability of the solid flow field, the weaker the erosion wear effect of the particles on the wall surface. The change in fluid velocity in the throttling area of the high-pressure black water angle valve is the most intense, and the stability of the flow field is worse than that in the other areas. Therefore, the erosion damage to the valve body in this area is also the most serious. Figures 13–16 show different valve cavity radius throttling area velocity vector amplification diagrams for 20%, 40%, 60%, and 80% opening degrees. The figure shows that the radius of the 40% opening valve chamber is 132 mm and the radius of the 60% opening valve chamber is 129 mm. Although the velocity variation amplitude of the two, the latter has an obvious fluid bias phenomenon, and its flow field stability is low. The fluid bias flow affects the velocity distribution uniformity of the flow field and the angle of the impact wall, which in turn affects the erosion wear. A comprehensive analysis of Figs. 13–16 shows that, under different openings and valve chamber radii, the fluid has different degrees of bias in the throttling area, which causes different degrees of disturbance to the flow field. With an increase of the valve opening, the maximum flow velocity of the fluid decreases continuously, and the degree of fluid deviation gradually weakens. At a larger opening of 80%, the flow field in the throttling area is close to the symmetrical flow field, and the flow field stability is the highest.

To compare and analyze the degrees of deviation of the throttling area quantitatively, a calculation deviation index (D_i) is proposed. The larger the value of D_i, the greater the degree of fluid deviation in the throttling area. To compare and analyze the differences in the degree of fluid deviation in the throttling zone, the velocity and position information of 200 points on the middle position line from the top of the spool to the outlet of the valve seat shown in Fig. 18(a) were uniformly extracted, and the drift index D_i of the fluid velocity distribution was calculated according to Equation (22).

$$D_i = \sqrt{\frac{\sum_{i=1}^{N}[(u_i d_i - \bar{u} d_i)/\bar{u}]^2}{N}} \tag{22}$$

where u_i is the flow velocity of the point (m/s), $\bar{u}$ is the average velocity value of the point (m/s), $d_i = |x_i|/|x_i|_{max}$, is the offset of the selected point, x_i is the coordinate of the selected point in the *x*-axis direction (mm), and $d_i = |x_i|/|x_i|_{max}$ is the offset of the selected point, n = 1, 2,..., 199, 200, N = 200.

Figure 18 shows the variation curve of the D_i value of throttling area with respect to the radius of the valve chamber under different openings. The analysis shows that, with an increase in the radius of the valve cavity, the

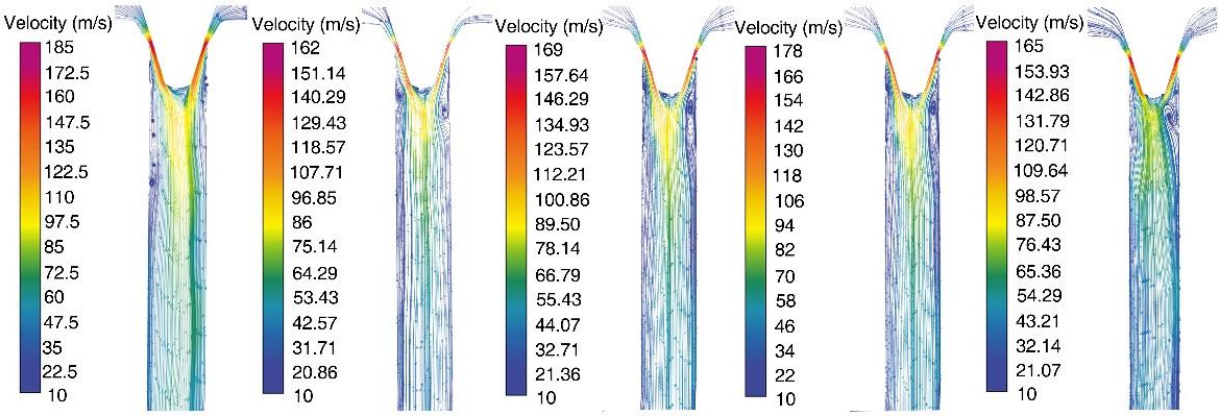

(a) 129 mm (b) 132 mm (c) 135 mm (d) 138 mm (e) 141 mm

Fig. 14 Amplification diagram of medium velocity vector in 20% opening throttle area

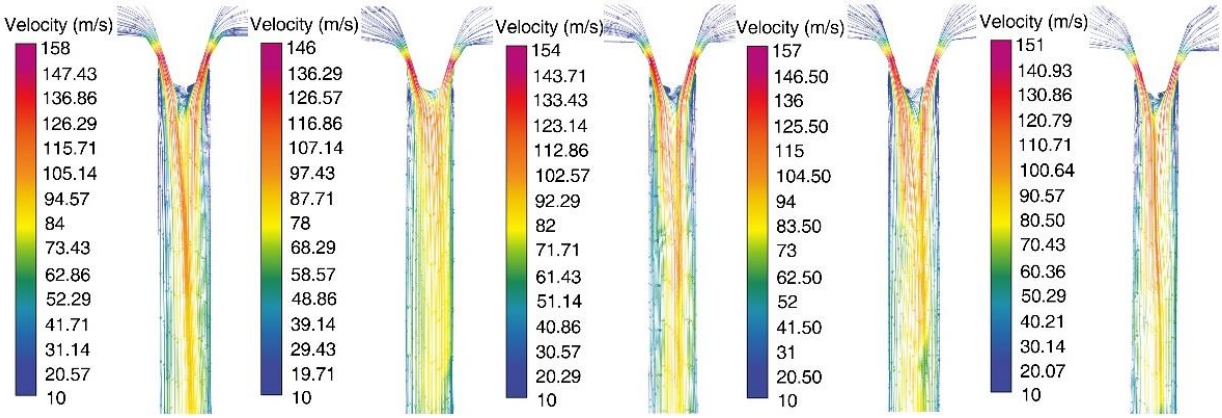

(a) 129 mm (b) 132 mm (c) 135 mm (d) 138 mm (e) 141 mm

Fig. 15 Amplification diagram of medium velocity vector in 40% opening throttle area

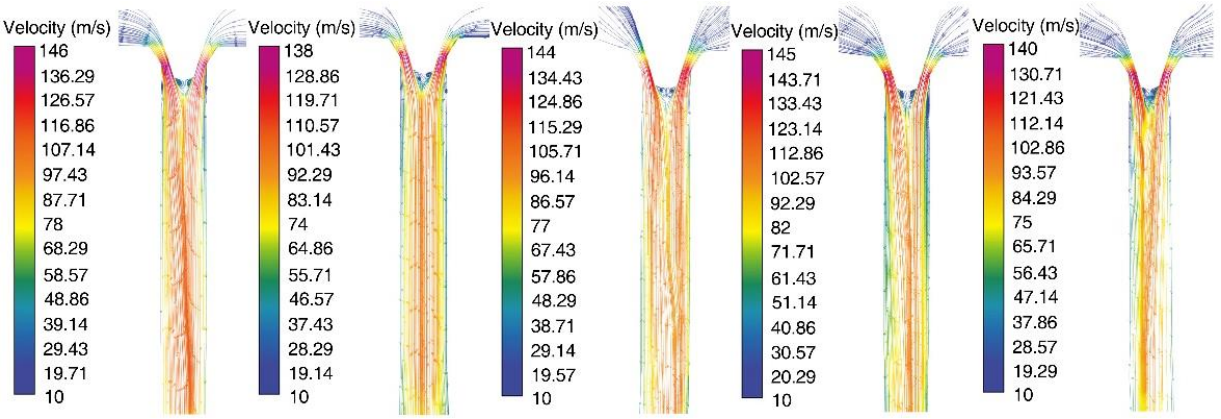

(a) 129 mm (b) 132 mm (c) 135 mm (d) 138 mm (e) 141 mm

Fig. 16 Amplification diagram of medium velocity vector in 60% opening throttle area

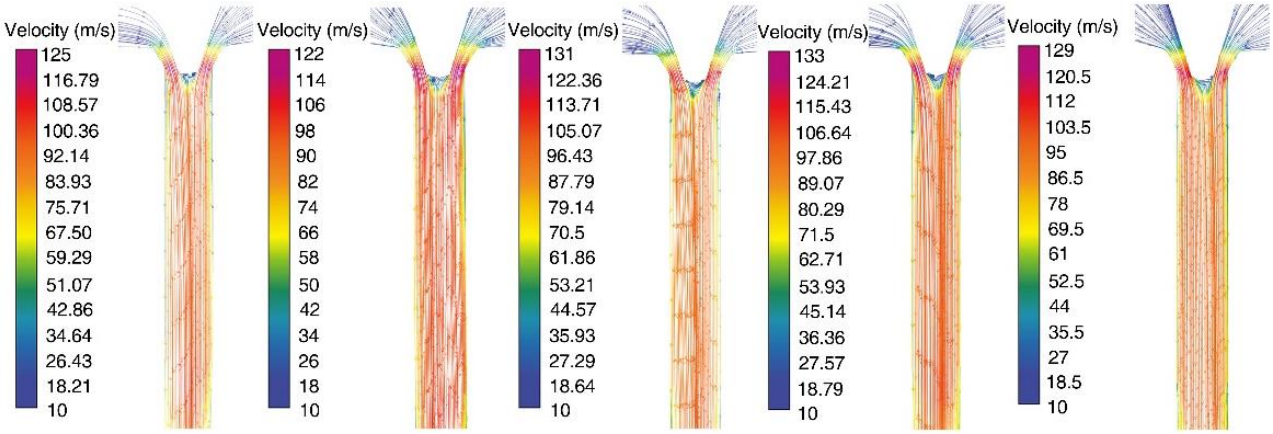

(a) 129 mm (b) 132 mm (c) 135 mm (d) 138 mm (e) 141 mm

Fig. 17 Amplification diagram of medium velocity vector in 80% opening throttle area

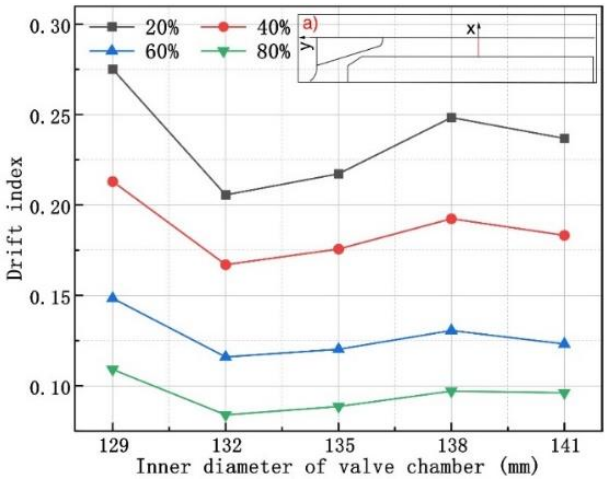

Fig. 18 Variation of the fluid drift index of the throttling area with the radius of the same valve chamber at different openings

degree of fluid deviation first decreases and then increases. The influence of the valve cavity radius gradually decreases with an increase in the valve opening. A comparative analysis shows that the valve cavity radius significantly influences the deviation of the fluid in the throttling area. For example, when the opening degree is 20%, the maximum difference in the deviation index of the fluid under different valve cavity radii is 0.7; however, the minimum drift index of the fluid is only 0.8 at 80% opening. When the valve cavity radius is 132 mm, the offset index value of the fluid in the throttling area is the smallest, and the flow field stability is the strongest. According to the variation curve of the maximum flow velocity and the deviation index of the throttling area, a valve cavity radius of 132 mm is the best value in the range of valve cavity radius studied.

4.3 Erosion Wear Characteristics

The above analysis reveals that, owing to the differences in velocity and stability in different regions of the flow field, the valve body has different degrees of erosion wear damage. Furthermore, under the influence of a large velocity gradient and pressure gradient, the particles rebound with the high-speed impact of the fluid on the valve core head and valve seat wall, resulting in serious erosion wear damage. Figures 19–22 and 23–26 show erosion wear rate distribution nephograms of the valve core head and valve seat under different opening degrees and different valve cavity radii, respectively. The analysis shows that the high wear rate is mainly concentrated at the head of the valve core, orifice of the valve seat, and outlet of the valve seat. The wear of the valve core is more severe than that of the valve seat. Under different valve openings, the wear rate of the valve core is in the order of 1E-6-1E-5 $kg/m^2 \cdot s$, and the wear rate of the valve seat wall is in the order of 1E-7-1E-6 $kg/m^2 \cdot s$. Under the conditions of extreme opening (20%) and large opening (80%), the erosion wear rate of the spool head is one order of magnitude higher than that of the valve seat.

Along the flow direction of the fluid, the gas content in the valve seat near the wall gradually increases. The collapse of the gas phase on the valve seat wall enhances the impact of the particles on the wall. Therefore, a position with a higher valve seat wear rate appears in the transition wall and outlet area. With an increase in the opening, the wear rate of the valve internals decreases gradually. There is no significant difference in the position of the wear rate distribution of the valve under different valve cavity structures and valve openings. The variations in the wear rate of the valve internals with the radius of the valve cavity under different opening conditions are basically the same. of the contents of Sections 4.1 and 4.2 show that, the larger the valve opening, the weaker the impact of the particles on the valve internals. The erosion wear rate values obtained by the numerical calculations are also smaller. Figures 19–26 reveal that the proportion of the high wear rate area first decreases, then increases, and then decreases with a change in the valve cavity radius. When the radius of the valve cavity is 132 mm, the proportion of high wear rate is the smallest, and the overall erosion wear rate is small.

The average erosion wear rate of the valve internals in the throttling area changes with the radius of the valve chamber, as shown in Fig. 27. The analysis indicates that, as the opening increases, the influence of the valve

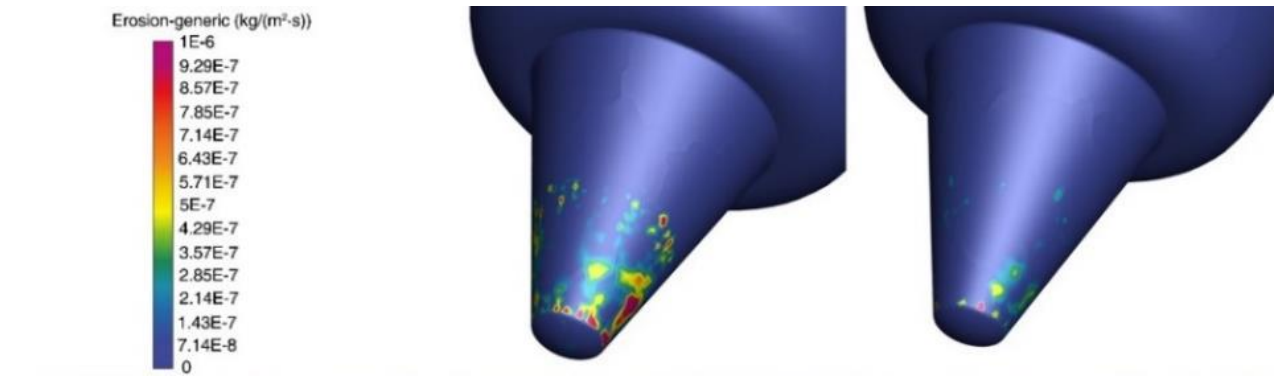

(a) 129 mm (b) 132 mm

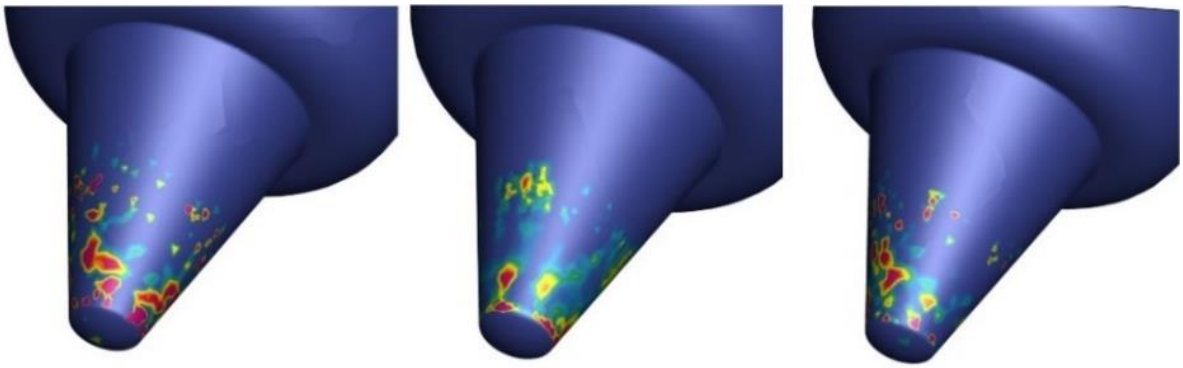

(c) 135 mm (d) 138 mm (e) 141 mm

Fig. 19 Distribution cloud diagram of wear rate of valve core head at 20% opening

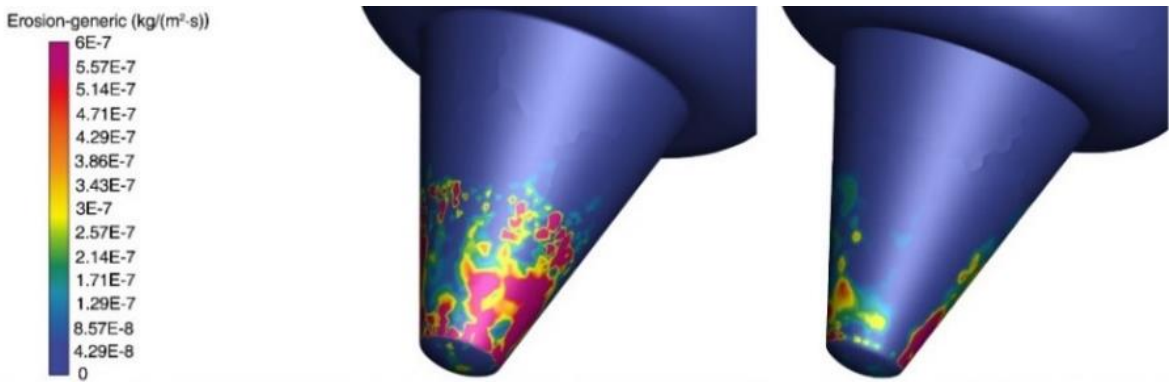

(a) 129 mm (b) 132 mm

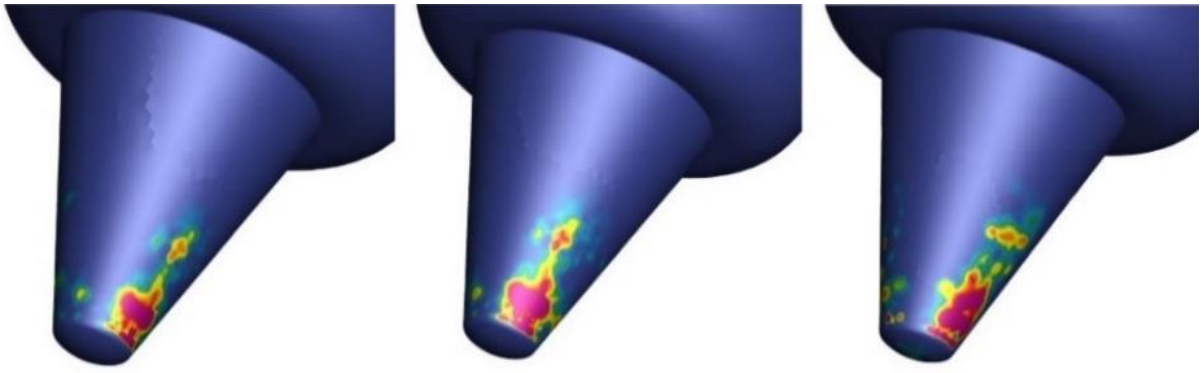

(c) 135 mm (d) 138 mm (e) 141 mm

Fig. 20 Distribution cloud diagram of wear rate of valve core head at 40% opening

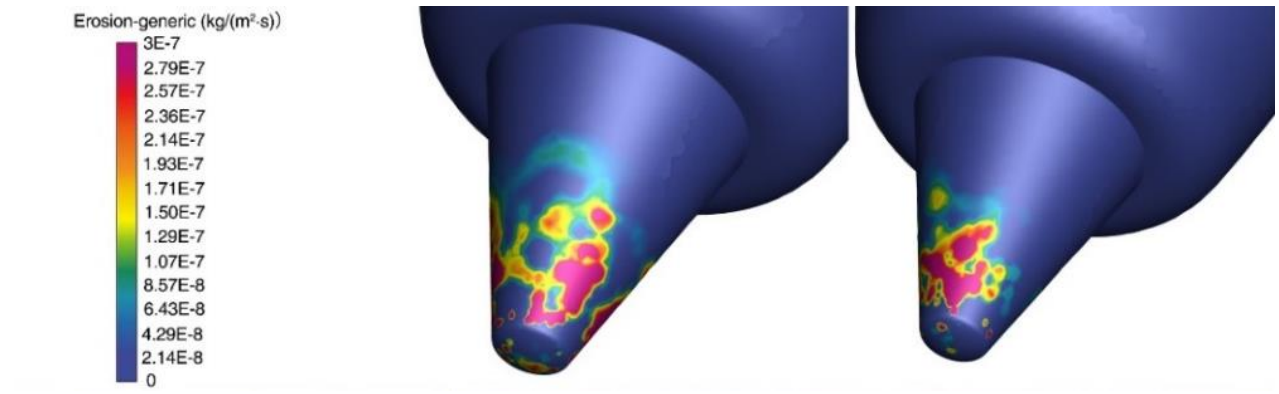

(a) 129 mm (b) 132 mm

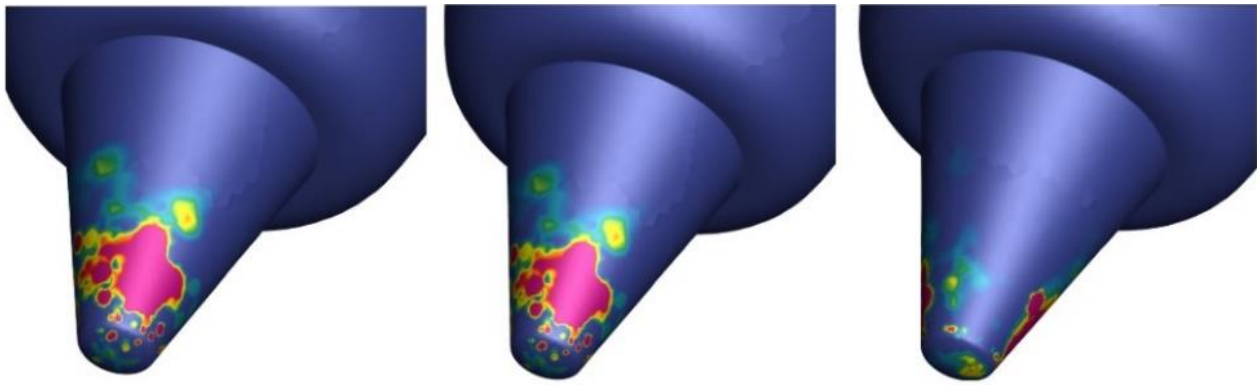

(c) 135 mm (d) 138 mm (e) 141 mm

Fig. 21 Distribution cloud diagram of wear rate of valve core head at 60% opening

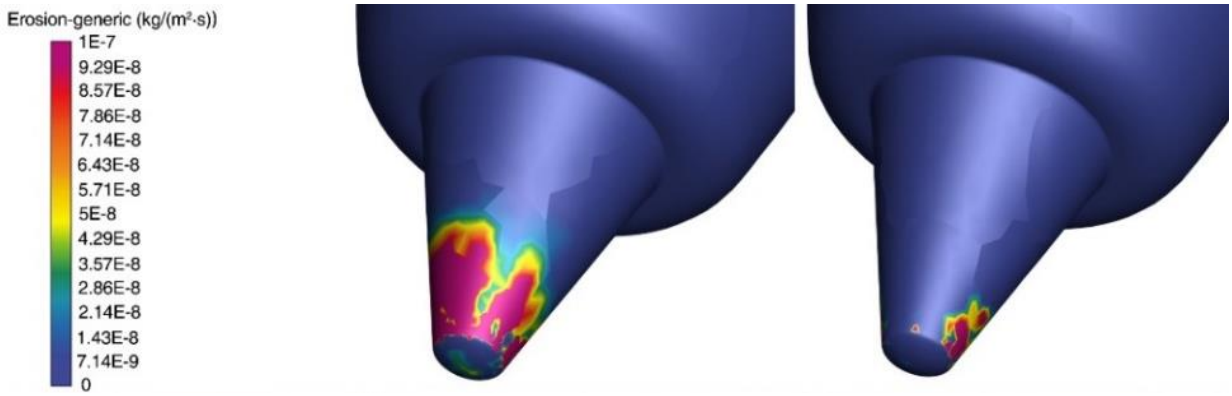

(a) 129 mm (b) 132 mm

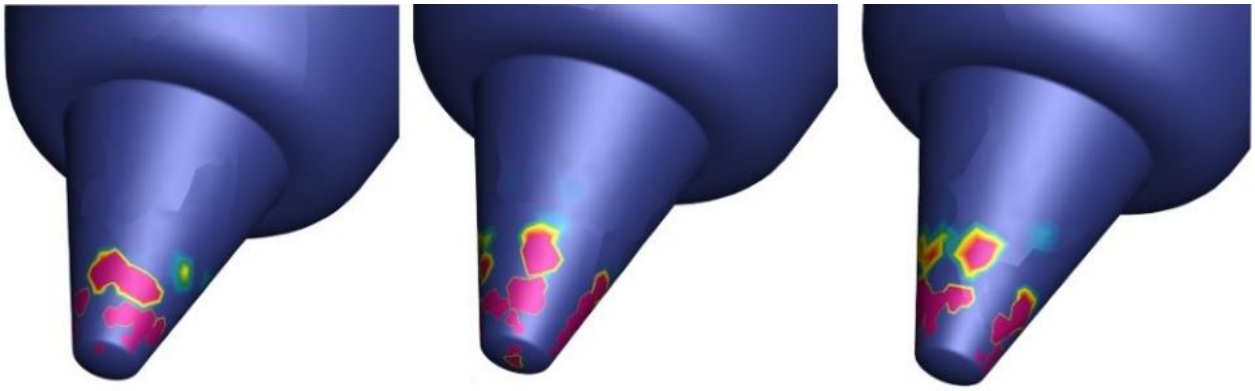

(c) 135 mm (d) 138 mm (e) 141 mm

Fig. 22 Distribution cloud diagram of wear rate of valve core head at 80% opening

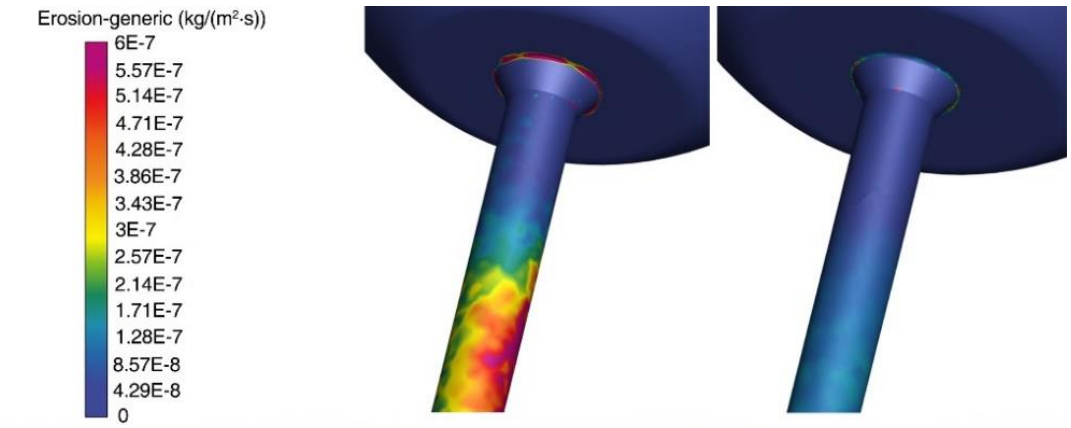

(a) 129 mm (b) 132 mm

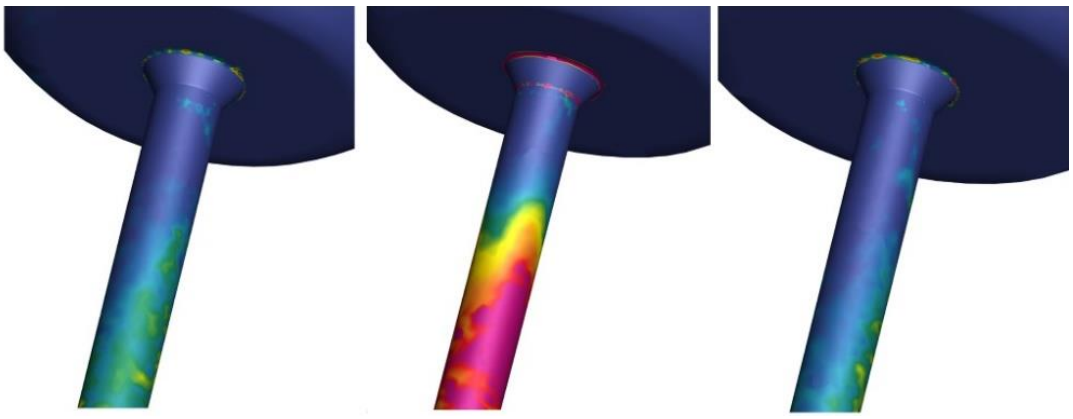

(c) 135 mm (d) 138 mm (e) 141 mm

Fig. 23 Distribution cloud diagram of wear rate of valve seat at 20% opening

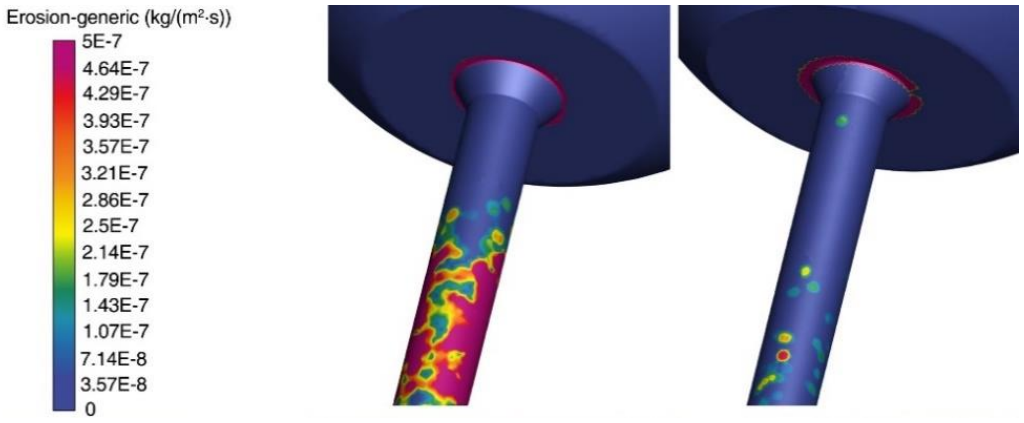

(a) 129 mm (b) 132 mm

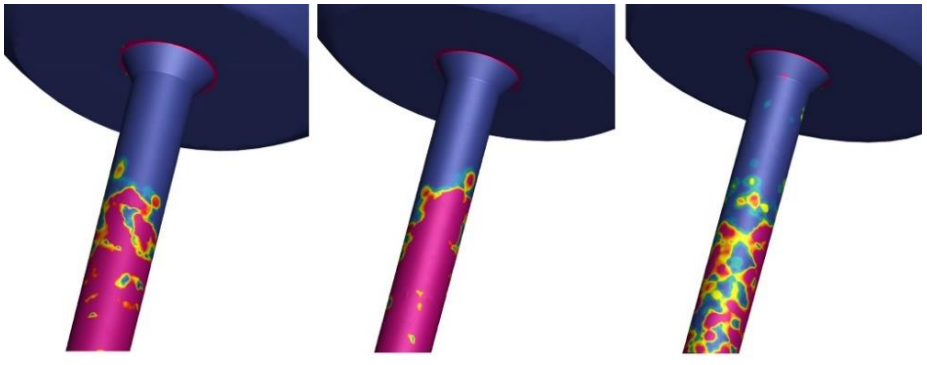

(c) 135 mm (d) 138 mm (e) 141 mm

Fig. 24 Distribution cloud diagram of wear rate of valve seat at 40% opening

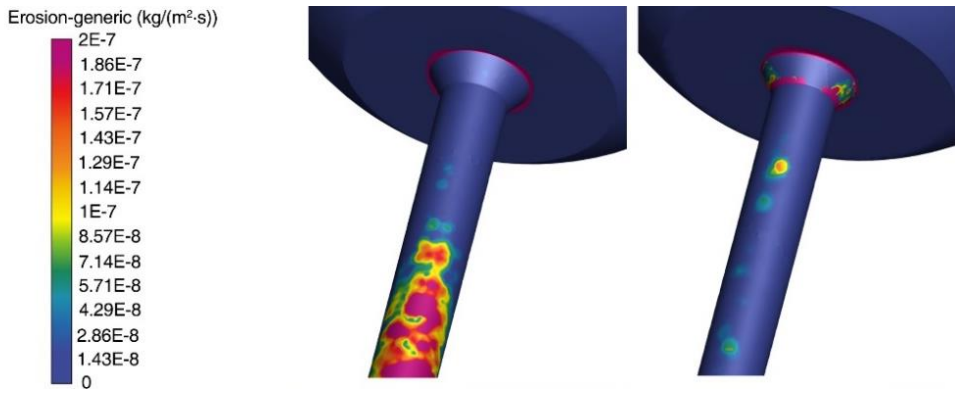

(a) 129 mm (b) 132 mm

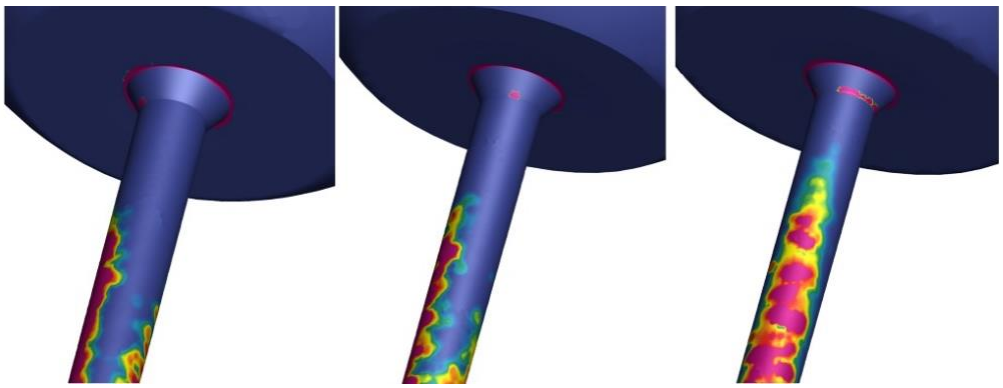

(c) 135 mm (d) 138 mm (e) 141 mm

Fig. 25 Distribution cloud diagram of wear rate of valve seat at 60% opening

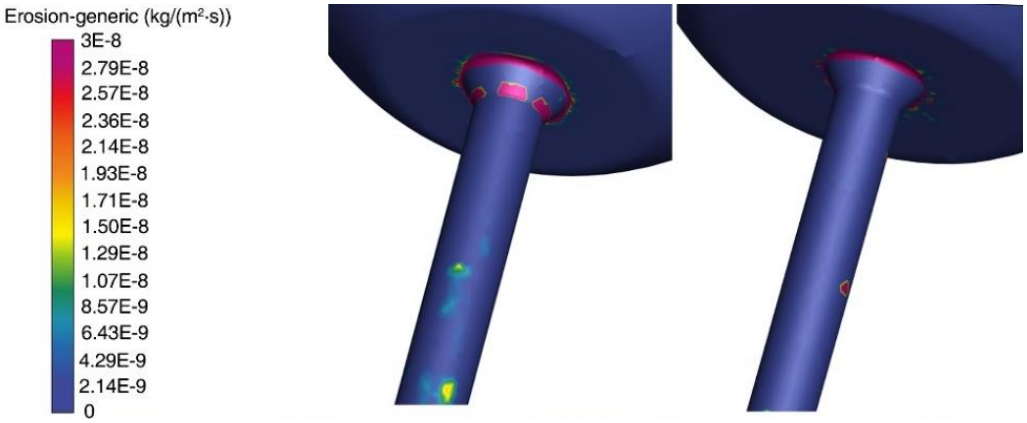

(a) 129 mm (b) 132 mm

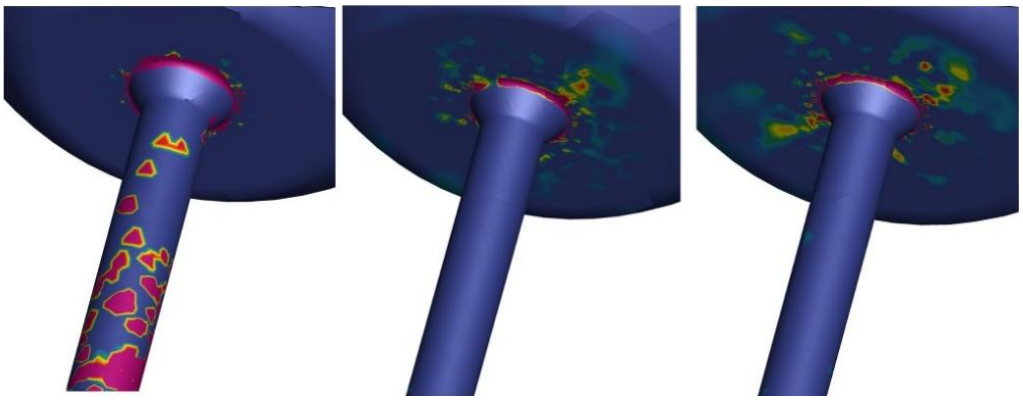

(c) 135 mm (d) 138 mm (e) 141 mm

Fig. 26 Distribution cloud diagram of wear rate of valve seat at 80% opening

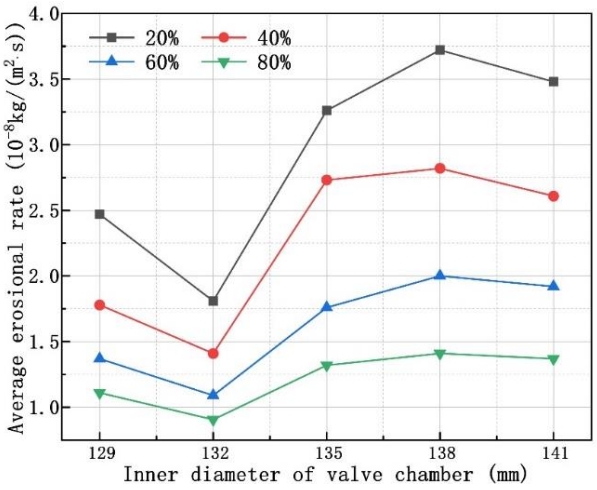

Fig. 27 Variation in the average wear rate on the inner wall of the valve with the radius of the valve cavity under different opening degrees

chamber radius on the wear rate of the valve internals gradually weakens. When the radius of the valve cavity is larger, the maximum wear rate changes more smoothly for the same opening. Therefore, the valve cavity radius significantly affects the erosion wear of the particles on the valve internals. For example, under openings of 20%, 40%, 60%, and 80%, the maximum differences in the average wear rate caused by different valve chamber radii are 1.92, 1.40, 0.91, and 0.50 E-8 kg/m^2 · s, respectively. The ratios of the values to the maximum values of the average wear rate under the same opening are 0.45, 0.5, 0.46, and 0.36, respectively. The erosion wear strength is reduced significantly.

The pressure-regulating ability of the valve is inversely proportional to the severity of the erosion wear of the valve internals. Therefore, erosion wear seriously threatens the efficiency of the black water treatment system and the safety of the coal gasification process. The analysis in this section reveals that, when the valve cavity radius is 132 mm, the erosion wear damage of the valve internals can be reduced by nearly half compared with other values. This can prolong the service life of the valve under the same operating conditions.

5. CONCLUSIONS

In the depressurization and flash evaporation of high-temperature black water, the flow field distribution in the valve is extremely complex, and the erosion wear problem of the valve internals is usually serious. In this study, the CFD-VOF-DPM method was used to visualize the internal flow field of the valve. The variation laws under different radii of the valve cavity and opening degrees were determined, and the main conclusions are as follows.

(1) The instantaneous pressure drop is the driving force for large-area flashing in the valve. The greater the flashing intensity of the flow field, the more disordered the flow field. The gas volume fraction is proportional to the flash intensity, which increases with increasing valve cavity radius. The evaporation intensity of the valve is the lowest when the valve chamber radius is 132 mm. Under openings of 20%, 40%, 60%, and 80%, the maximum differences in gas volume fraction under different valve chamber radii are 14.98%, 10.27%, 9.18%, and 7.62%, respectively.

(2) The fluid flows most strongly in the throttling area, and there are different degrees of bias flow that cause different degrees of disturbance to the flow field. There are significant differences in the drift index and maximum flow velocity of the flow field for different openings and valve chamber radii. In addition, the maximum differences under openings of 20%, 40%, 60%, and 80% are 0. 069, 20 m/s; 0.046, 12 m/s; 0.033, 8 m/s; and 0.025, 11 m/s, respectively. For an 80% opening, the minimum drift index of the fluid is only 0.084. When the radius of the valve chamber is 132 mm, the drift index of the fluid in the throttling area is the smallest, and the influence of the fluid on the impact of the solid particles and wall surface is the smallest under this structural condition.

(3) When the flow medium flows through the throttling area, the solid particles impact and rebound at a higher collision angle between the valve head and the valve seat. Under different valve cavity radii, the average wear rates of the valve body wall in the throttling area differ significantly. In the range of the valve cavity radii investigated in this study, the average wear rate is the smallest when the valve cavity radius is 132 mm. The ratios of the maximum differences in the average wear rates of 20%, 40%, 60%, and 80% to the maximum average wear rate are 0.45, 0.5, 0.46, and 0.36, respectively.

The valve chamber radius of the high-pressure black water angle valve has a significant influence on the flow characteristics of the flow field in the valve, which in turn affects the erosion wear effect of the medium in the valve on the inner parts of the valve. In the value range of the valve cavity radius investigated, when the valve cavity radius value is 132 mm, the erosion wear damage of the valve internals can be reduced by nearly half compared with other radius values, and the service life of the valve can be extended under the same operating conditions. Under the premise of not changing the structure, the valve cavity radius value is reasonably selected in combination with the production cost. This can improve the flow characteristics of the high-pressure black water angle valve and its operational reliability.

ACKNOWLEDGMENTS

This work was supported by the National Natural Science Foundation of China (Grants No. 52176048, No. 51876194, and No. U1909216). The authors are grateful for this support.

CONFLICT OF INTEREST

The authors report that there are no competing interests to declare.

AUTHOR CONTRIBUTIONS

Haozhe Jin: Methodology, Resources, Writing – Review & Editing, Supervision. **Hengyang Xiang:** Conceptualization, Software, Validation, Visualization, Writing – Original Drafting, Writing – Review & Editing. **Mingxiang Wang:** Writing – Review & Editing. **Ruoshuang Wen:** Writing – Review & Editing. **Xiaofei Liu:** Supervision, Writing – Review & Editing. **Chao Wang:** Conceptualization, Supervision, Writing – Review & Editing.

REFERENCES

Abbaspour, M., Chapman, K. S., Glasgow, L. A., & Zheng, Z. C. (2005). *Dynamic simulation of gas-liquid homogeneous flow in natural gas pipeline using two-fluid conservation equations*. ASME 2005 Fluids Engineering Division Summer Meeting, 787-795. https://doi.org/10.1115/FEDSM2005-77136

Alghurabi, A., Mohyaldinn, M., Jufar, S., Younis, O., Abduljabbar, A., & Azuwan, M. (2021). CFD numerical simulation of standalone sand screen erosion due to gas-sand flow. *Journal of Natural Gas Science and Engineering*, *85*, 103706. https://doi.org/10.1016/j.jngse.2020.103706

Bambhania, M., & Patel, N. K. (2022). Numerical modeling of the cavitation flow in throttle geometry. *Journal of Applied Fluid Mechanics*, *16*(2), 257-267. https://doi.org/10.47176/jafm.16.02.1348

Ban, S., Pao, W., & Nasif, M. S. (2021). Experimental and CFD investigations of 45 and 90 degrees bends and various elbow curvature radii effects on solid particle erosion. *Wear*, *476*, 203646. https://doi.org/10.1016/j.wear.2021.203646

Cao, L., Liu, S., Hu, P., & Si, H. (2020). The influence of governing valve opening on the erosion characteristics of solid particle in steam turbine. *Engineering Failure Analysis*, *118*, 104929. https://doi.org/10.1016/j.engfailanal.2020.104929

Chen, P., Cui, B., Li, J., Zheng, J., & Zhao, Y. (2022). Particle erosion under multiphase bubble flow in horizontal-vertical-upward elbows. *Powder Technology*, *397*, 117002. https://doi.org/10.1016/j.powtec.2021.11.046

Chen, S., Gong, J., Li, W., Yang, Q., Shi, G., Li, X., Shi, B., Song, S., Lv, P., Fan, Di., & Duan, X. (2021). A new transient model of multi-scale bubble migration and evolution during gas-liquid flow in pipelines. *Journal of Petroleum Science and Engineering*, *205*. https://doi.org/10.1016/j.petrol.2021.108888

Chowdhury, M. A., Hossain, N., Shahin, M., Debnath, U. K., Rahman, M., & Rahman, M. M. (2022). Erosion characteristics of stainless steels under different percentage of SiC-Al2O3-Fe2O3 solid particles. *Tribology International*, *167*, 107403. https://doi.org/10.1016/j.triboint.2021.107403

Drew, D., Cheng, L., & Lahey Jr, R. T. (1979). The analysis of virtual mass effects in two-phase flow. *International Journal of Multiphase Flow*, *5*(4), 233-242. https://doi.org/10.1016/0301-9322(79)90023-5

Espinoza-Jara, A., Walczak, M., Molina, N., Jahn, W., & Brevis, W. (2022). Erosion under turbulent flow: a CFD-based simulation of near-wall turbulent impacts with experimental validation. *Engineering Applications of Computational Fluid Mechanics*, *16*(1), 1526-1545. https://doi.org/10.1080/19942060.2022.2099978

Forder, A., Thew, M., & Harrison, D. (1998). A numerical investigation of solid particle erosion experienced within oilfield control valves. *Wear*, *216*(2), 184-193. https://doi.org/10.1016/S0043-1648(97)00217-2

Ganesan, P. B., Tariqul Islam, M., Pokrajac, D., Hamad, F. A., & Sandaran, S. C. (2017). Coalescence and rising behavior of co ‐ axial and lateral bubbles in viscous fluid: a CFD study. *Asia-Pacific Journal of Chemical Engineering*, *12*, 605-619. https://doi.org/10.1002/apj.2102

Guo, F., Guo, Y., Qiu, G., Xu, J., Niu, Y., Zhang, Y., Jiang, L., Hu, X., Wu, J., & Zhang, H. (2022). A new separation flowsheet for resources recovery from waste coal gasification fine slag black water and its benefits analysis. *Process Safety and Environmental Protection*, *164*, 836-845. https://doi.org/10.1016/j.psep.2022.06.049

Hou, L. Y., Wang, K. S., & Lu, T. (2011). *Simulation study of fluid flowing and cavitation in high-pressure regulator valve*. International Conference on Consumer Electronics, Communications and Networks (CEC Net), 2613-2616. https://doi.org/10.1109/CECNET.2011.5768676

Humphrey, J. A. C. (1990). Fundamentals of fluid motion in erosion by solid particle impact. International *Journal of Heat and Fluid Flow*, *11*(3), 170-195. https://doi.org/10.1016/0142-727X(90)90036-B

Kharangate, C. R., & Mudawar, I. (2017). Review of computational studies on boiling and condensation. *International Journal of Heat and Mass Transfer*, *108*, 1164-1196. https://doi.org/10.1016/j.ijheatmasstransfer.2016.12.065

Kou, B., Hou, Y., Fu, W., Yang, N., Liu, J., & Xie, G. (2023). Simulation of Multi-Phase flow in autoclaves using a coupled CFD-DPM Approach. *Processes*, *11*(3), 890. https://doi.org/10.3390/pr11030890

Li, L., Gu, Z., Xu, W., Tan, Y., Fan, X., & Tan, D. (2023). Mixing mass transfer mechanism and dynamic control of gas-liquid-solid multiphase flow based on VOF-DEM coupling. *Energy*, *272*, 127015. https://doi.org/10.1016/j.energy.2023.127015

Li, Y., Zhang, J., & Fan, L. S. (1999). Numerical simulation of gas–liquid–solid fluidization systems using a combined CFD-VOF-DPM method: bubble wake behavior. *Chemical Engineering Science*,

54(21), 5101-5107. https://doi.org/10.1016/S0009-2509(99)00263-8

Mansouri, A., Arabnejad, H., Shirazi, S. A., & McLaury, B. S. (2015). A combined CFD/experimental methodology for erosion prediction. *Wear, 332*, 1090-1097. https://doi.org/10.1016/j.wear.2014.11.025

Parsi, M., Najmi, K., Najafifard, F., Hassani, S., McLaury, B. S., & Shirazi, S. A. (2014). A comprehensive review of solid particle erosion modeling for oil and gas wells and pipelines applications. *Journal of Natural Gas Science and Engineering*, *21*, 850-873. https://doi.org/10.1016/j.jngse.2014.10.001

Peng Jr, D., Pak, A., Chinello, L., Wood, T., & Low, A. (2013). *Advances in Multiphase Flow CFD Erosion Analysis.* Offshore Technology Conference, OTC-24114-MS. https://doi.org/10.4043/24114-MS

Qin, D., Pan, G., Huang, Q., Zhang, Z., & Ke, J. (2018). Numerical investigation of different tip clearances effect on the hydrodynamic performance of pumpjet propulsor. *International Journal of Computational Methods*, *15*(05), 1850037. https://doi.org/10.1142/S0219876218500378

Severiano, J. D., Silva, A. S., Sussushi, E. M., da Silva Sant'Anna, M. V., da Cunha, M. A., Bergmann, C. P., & Griza, S. (2019). Corrosion damages of flow regulation valves for water injection in oil fields. *Engineering Failure Analysis*, *96*, 362-373. https://doi.org/10.1016/j.engfailanal.2018.11.002

Shao, C., Ge, Z., Zhou, Z., Liu, W., Li, Z., Tian, C. & Chang, W. (2023). Experimental and numerical investigation of abrasive water jet nozzle erosion. *Powder Technology*, *430*, 119031. https://doi.org/10.1016/j.powtec.2023.119031

Shirani, E., Ghadiri, F., & Ahmadi, A. (2011). Modeling and simulation of interfacial turbulent flows. *Journal of Applied Fluid Mechanics*, 43-19. https://doi.org/10.36884/jafm.4.03.11933

Song, X., Cui, L., Cao, M., Cao, W., Park, Y., & Dempster, W. M. (2014). A CFD analysis of the dynamics of a direct-operated safety relief valve mounted on a pressure vessel. *Energy Conversion and Management*, *81*, 407-419. https://doi.org/10.1016/j.enconman.2014.02.021

Tan, D. P., Ni, Y. S., & Zhang, L. B. (2017). Two-phase sink vortex suction mechanism and penetration dynamic characteristics in ladle teeming process. *Journal of Iron and Steel Research, International*, *24*(7), 669-677. https://doi.org/10.1016/S1006-706X(17)30101-2

Wang, S., & Shen, Y. (2023). CFD-DEM-VOF-phase diagram modelling of multi-phase flow with phase changes. *Chemical Engineering Science*, *273*, 118651. https://doi.org/10.1016/j.ces.2023.118651

Wallace, M. S., Dempster, W. M., Scanlon, T. J., Peters, J., & Mcculloch, S. (2004). Prediction of impact erosion in valve geometries. *Wear*, 256, 927-936. https://doi.org/10.1016/j.wear.2003.06.004

Wen, Q., Liu, Y., Chen, Z., & Wang, W. (2022). Numerical simulation and experimental validation of flow characteristics for a butterfly check valve in small modular reactor. *Nuclear Engineering and Design*, *391*, 111732. https://doi.org/10.1016/j.nucengdes.2022.111732

Wiedemann, P., Meller, R., Schubert, M., & Hampel, U. (2023). Application of a hybrid multiphase CFD approach to the simulation of gas–liquid flow at a trapezoid fixed valve for distillation trays. *Chemical Engineering Research and Design*, *193*, 777-786. https://doi.org/10.1016/j.cherd.2023.04.016

Yadigaroglu, G., & Zeller, M. (1994). Fluid-to-fluid scaling for a gravity- and flashing-driven natural circulation loop. *Nuclear Engineering and Design*, *151*(1), 49-64. https://doi.org/10.1016/0029-5493(94)90033-7

Yan, X., Wei, W., You, M., Fan-Ding, L., & Hao-Zhe, J. (2021). The impact of inlet flash evaporation conditions on erosion damage characteristics of coal gasification black water angle valve and prevention strategies. *Mechanics & Industry*, *21*(6), 626. https://doi.org/10.1051/meca/2020092

Yu, R., Wu, Y., Chen, X., & Wu, X. (2023). Study on the design of ball valve based on elastic ring valve seat structure and fluid characteristics and fatigue strength. *Flow Measurement and Instrumentation*, *89*, 102302. https://doi.org/10.1016/j.flowmeasinst.2022.102302

Zamani, M., Seddighi, S., & Nazif, H. R. (2017). Erosion of natural gas elbows due to rotating particles in turbulent gas-solid flow. *Journal of Natural Gas Science and Engineering*, *40*, 91-113. https://doi.org/10.1016/j.jngse.2017.01.034

Zhang, E., Zeng, D., Zhu, H., Li, S., Chen, D., Li, J., Ding, Y., & Tian, G. (2018). Numerical simulation for erosion effects of three-phase flow containing sulfur particles on elbows in high sour gas fields. *Petroleum*, *4*(2), 158-167. https://doi.org/10.1016/j.petlm.2017.12.008

Zhang, M. M., Katz, J., & Prosperetti, A. (2010). Enhancement of channel wall vibration due to acoustic excitation of an internal bubbly flow. *Journal of Fluids and Structures*, *26*(6), 994-1017. https://doi.org/10.1016/j.jfluidstructs.2010.06.003

Zheng, K., Hu, H., Chen, F., & Zheng, Y. (2021). Failure analysis of the blackwater regulating valve in the coal chemical industry. *Engineering Failure Analysis*, *125*, 105442. https://doi.org/10.1016/j.engfailanal.2021.105442

Zheng, Z., Ou, G., Yi, Y., Shu, G., Jin, H., Wang, C., & Ye, H. (2016). A combined numerical-experiment investigation on the failure of a pressure relief valve in coal liquefaction. *Engineering Failure Analysis*, *60*, 326-340. https://doi.org/10.1016/j.engfailanal.2015.11.055